International Forum on Aeroelasticity and Structural Dynamics
IFASD 2017
25-28 June 2017 Como, Italy

FLUTTER ANALYSIS FOR THE SECOND AEROELASTIC PREDICTION WORKSHOP

Daniella E. Raveh[1]

[1]Faculty of Aerospace Engineering
Technion - Israel Institute of Technology
Haifa, Israel
daniella@technion.ac.il

Keywords: Flutter Analysis, Aeroelastic Prediction Workshop

Abstract: The paper presents flutter prediction and simulations that were performed with the EZNSS flow solver for the second Aeroelastic Prediction Workshop (AePW). The reference test cases for the AePW are based on two wind tunnel experiments of the Benchmark Supercritical Wing (BSCW). Two cases are addressed, at different transonic flow conditions: One case at lower Mach numbers of 0.74, 0°angle of attack (AoA), and one more physically complex case at Mach 0.85, 5°AoA. The cases were analyzed with the EZNSS code, using several computational setups and turbulence models. The simulations at Mach 0.74 0°AoA were able to predict accurately the flutter response. A reduced-order model (ROM) for the unsteady aerodynamic forces was constructed and used to predict the flutter point. The ROM was shown to be an accurate and computationally efficient tool for flutter prediction. The higher Mach number case, at Mach 0.85, 5°AoA, which involves a strong shock, separated flow behind the shock, and some flow unsteadiness, was more challenging. In the static analysis, different turbulence models yielded different upper-surface shock positions, and none of the models was able to capture accurately the pressure recovery behind the shock. Flutter was computed via an aerodynamic ROM, and since there is no reference flutter point from wind tunnel tests, the flutter point was validated with full aeroelastic simulation.

1 INTRODUCTION

The accurate computation of aeroelastic responses and unsteady aerodynamic forces due to structural motion is of great importance to aircraft aeroelastic analysis and structural design. The Aeroelastic Prediction Workshop (AePW) series, taking after the Drag and High-lift Prediction Workshops, addresses these topics. The AePW aims at assessment of state-of-the-art CFD codes simulating flow-fields about wings undergoing prescribed motions, or static and dynamic aeroelastic deformations, at transonic flight conditions. The first AePW [1] evaluated three configurations: The Rectangular Supercritical Wing (RSW), the Benchmark Supercritical Wing (BSCW), and the High Reynolds Number Aerostructural Dynamics (HIRENASD). The second AePW focuses on the BSCW, and includes computation of unsteady aerodynamic pressures in response to prescribed motion, as well as simulation and prediction of flutter.

The BSCW is a semi-rigid, semispan, rectangular wing, with a chord of 0.4064 m (16 inches), a span of 0.8128 m (32 inches), and a SC(2)0414 supersonic airfoil (see figure 1). The test cases for the AePW are based on two wind tunnel experiments of the BSCW model that were conducted in the NASA Langley Transonic Dynamics Tunnel. The first experiment is a *flutter*

test, in which the semi-rigid wing was suspended from a pitch and plunge apparatus (PAPA), simulating two degrees-of-freedom flutter [2]. Reference data (for AePW purposes) includes experimental results in R-12 gas, at *Mach 0.74, 0°* angle of attack (AoA). The second experiment is a *forced excitation* test, in which the wing was oscillated in pitch, about an axis at the 30% chord, via an oscillating turn table (OTT). [3] Reference data includes experimental results in response to pitch excitation of 1°, 10 Hz, at two flow conditions: *Mach 0.7, 3°AoA*, and a more physically complex case at *Mach 0.85, 5°AoA*. The latter case was analyzed also at the first AePW. Due to its complexity it is revisited in the second AePW as an optional case.

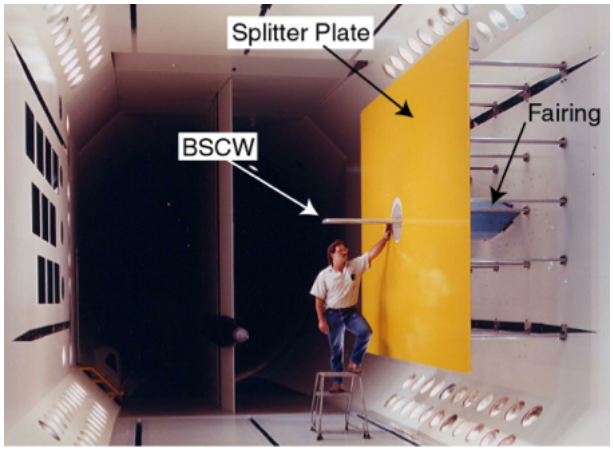

Figure 1: BSCW mounted in wind-tunnel (taken from Ref. [4])

The paper presents simulations of AePW cases preformed with EZNSS, an in-house code of the Israeli CFD center. The EZNSS code is a multi-zone Euler/Navier-Stokes flow solver. The code is capable of simulating complex, time-accurate flows about dynamically deforming geometries. This includes relative motion between surfaces, as well as deformations due to aeroelastic effects. The code offers a number of implicit algorithms and a number of turbulence models. It handles complex geometries using patched grids and the Chimera overset grid topology.

The current study focuses on flutter simulation and prediction at *Mach 0.74, 0°AoA* (with wind-tunnel test reference), and at *Mach 0.85, 5°AoA* (without wind-tunnel reference). Flutter dynamic pressure is evaluated based on an unsteady aerodynamic reduced-order model (ROM), following Ref. [5], and validated via aeroelastic simulation.

2 GOVERNING EQUATIONS

The governing equations are obtained by Favre-averaging the Navier-Stokes equations and modeling the Reynolds stress tensor. In what follows, the symbol $(-)$ indicates non-weighted averaging, the symbol $(\sim)$ signifies Favre averaging, and the symbol $('')$ denotes Favre fluctuations. In a compact form, the mean-flow equations may be expressed in generalized coordinates and a strong conservation-law form as:

$$\frac{\partial \hat{\boldsymbol{Q}}}{\partial \tau} + \frac{\partial (\hat{\boldsymbol{E}}^c - \hat{\boldsymbol{E}}^d)}{\partial \xi} + \frac{\partial (\hat{\boldsymbol{F}}^c - \hat{\boldsymbol{F}}^d)}{\partial \eta} + \frac{\partial (\hat{\boldsymbol{G}}^c - \hat{\boldsymbol{G}}^d)}{\partial \zeta} = 0 \tag{1}$$

where τ denotes the time, and ξ, η, and ζ are the curvilinear coordinates. The vector $\hat{\boldsymbol{Q}}$ denotes the mean-flow dependent variables given as:

$$\hat{\boldsymbol{Q}} = \frac{\boldsymbol{Q}}{J} = \frac{1}{J}\left[\bar{\rho}, \bar{\rho}\tilde{u}, \bar{\rho}\tilde{v}, \bar{\rho}\tilde{w}, \tilde{e}\right]^T \tag{2}$$

where J is the Jacobian of the transformation. The fluid density is denoted by ρ, the triad (u, v, w) denotes the Cartesian velocity vector components, and e is the total energy. The mean-flow rotated convective fluxes are given by:

$$\hat{\boldsymbol{E}}^c = \frac{1}{J}\begin{bmatrix} \bar{\rho}\widetilde{U} \\ \bar{\rho}\tilde{u}\widetilde{U} + \xi_x\bar{p} \\ \bar{\rho}\tilde{v}\widetilde{U} + \xi_y\bar{p} \\ \bar{\rho}\tilde{w}\widetilde{U} + \xi_z\bar{p} \\ (\widetilde{e}+\bar{p})\widetilde{U} - \xi_t\bar{p} \end{bmatrix}, \quad \hat{\boldsymbol{F}}^c = \frac{1}{J}\begin{bmatrix} \bar{\rho}\widetilde{V} \\ \bar{\rho}\tilde{u}\widetilde{V} + \eta_x\bar{p} \\ \bar{\rho}\tilde{v}\widetilde{V} + \eta_y\bar{p} \\ \bar{\rho}\tilde{w}\widetilde{V} + \eta_z\bar{p} \\ (\widetilde{e}+\bar{p})\widetilde{V} - \eta_t\bar{p} \end{bmatrix}, \quad \hat{\boldsymbol{G}}^c = \frac{1}{J}\begin{bmatrix} \bar{\rho}\widetilde{W} \\ \bar{\rho}\tilde{u}\widetilde{W} + \zeta_x\bar{p} \\ \bar{\rho}\tilde{v}\widetilde{W} + \zeta_y\bar{p} \\ \bar{\rho}\tilde{w}\widetilde{W} + \zeta_z\bar{p} \\ (\widetilde{e}+\bar{p})\widetilde{W} - \zeta_t\bar{p} \end{bmatrix} \tag{3}$$

where p denotes the pressure, and U,V, and W denote the Contravariant velocity components given by the transformation:

$$\begin{bmatrix} \widetilde{U} - \xi_t \\ \widetilde{V} - \eta_t \\ \widetilde{W} - \zeta_t \end{bmatrix} = \begin{bmatrix} \xi_x & \xi_y & \xi_z \\ \eta_x & \eta_y & \eta_z \\ \zeta_x & \zeta_y & \zeta_z \end{bmatrix} \begin{bmatrix} \tilde{u} \\ \tilde{v} \\ \tilde{w} \end{bmatrix} \tag{4}$$

The mean-flow rotated diffusive flux vectors are given by:

$$\hat{\boldsymbol{E}}^d = \frac{1}{J}\begin{bmatrix} 0 \\ \xi_i(\bar{\tau}_{ix} - \widetilde{\mathfrak{R}}_{ix}) \\ \xi_i(\bar{\tau}_{iy} - \widetilde{\mathfrak{R}}_{iy}) \\ \xi_i(\bar{\tau}_{iz} - \widetilde{\mathfrak{R}}_{iz}) \\ \xi_i\beta_i \end{bmatrix}, \quad \hat{\boldsymbol{F}}^d = \frac{1}{J}\begin{bmatrix} 0 \\ \eta_i(\bar{\tau}_{ix} - \widetilde{\mathfrak{R}}_{ix}) \\ \eta_i(\bar{\tau}_{iy} - \widetilde{\mathfrak{R}}_{iy}) \\ \eta_i(\bar{\tau}_{iz} - \widetilde{\mathfrak{R}}_{iz}) \\ \eta_i\beta_i \end{bmatrix}, \quad \hat{\boldsymbol{G}}^d = \frac{1}{J}\begin{bmatrix} 0 \\ \zeta_i(\bar{\tau}_{ix} - \widetilde{\mathfrak{R}}_{ix}) \\ \zeta_i(\bar{\tau}_{iy} - \widetilde{\mathfrak{R}}_{iy}) \\ \zeta_i(\bar{\tau}_{iz} - \widetilde{\mathfrak{R}}_{iz}) \\ \zeta_i\beta_i \end{bmatrix} \tag{5}$$

where τ_{ij} and $\widetilde{\mathfrak{R}}_{ij} = \widetilde{u_i''u_j''}$, are the viscous stress tensor and Reynolds-stress tensor components, respectively. The terms β_i are given as follows:

$$\beta_i = \widetilde{u}\left(\bar{\tau}_{ix} - \widetilde{\mathfrak{R}}_{ix}\right) + \widetilde{v}\left(\bar{\tau}_{iy} - \widetilde{\mathfrak{R}}_{iy}\right) + \widetilde{w}\left(\bar{\tau}_{iz} - \widetilde{\mathfrak{R}}_{iz}\right) + (\bar{\kappa} + \bar{\kappa}_t)\frac{\partial \bar{T}}{\partial x_i} \tag{6}$$

with T denoting the temperature and $\bar{\kappa}$ and $\bar{\kappa}_t$ the molecular and the turbulent thermal conductivity, respectively. The mean-flow equations are closed using the equation of state for a perfect gas,

$$\bar{p} = (\gamma - 1)\left[\widetilde{e} - \frac{1}{2}\bar{\rho}\left(\tilde{u}^2 + \tilde{v}^2 + \tilde{w}^2\right)\right] \tag{7}$$

where γ is the ratio of specific heats.

The unknown Favre-Reynolds averaging stress tensor is modeled in this work using the Boussinesq hypothesis, via linear eddy viscosity modeling. Three linear eddy viscosity closure models were used in the current work, the two-equation k-ω-SST model by Menter [6], the two-equation k-ω-TNT model by Kok [7], and the Spalart & Allmaras (SA) model with the Edwards and Chandra modification [8].

3 NUMERICAL METHODS

3.1 Flow Solver

The governing equations are discretized using a finite difference method on a curvilinear coordinates computational mesh using the EZNSS code. The diffusive fluxes of the mean-flow

equations and of the turbulence model equations are discretized using second-order central differencing based on a full-viscous stencil. The convective flux vector of the mean-flow equations may be approximated by second-order central differencing via the Beam & Warming algorithm or by upwind schemes such as the flux vector splitting by Steger-Warming or by an approximate Riemann solver such as the HLLC [9] and the $AUSM^{+}$-up scheme [10]. The left and right states of the approximate Riemann solvers are evaluated using a third-order biased MUSCL scheme. The convective flux of the turbulence model is approximated by the HLLC scheme based on the passive scalar approach using a third-order biased MUSCL scheme. Time marching schemes are the first- and second-order implicit backward Euler method for steady state and unsteady flows (dual-time), respectively. The time marching scheme used for the turbulence models is the unconditionally positive-stable scheme developed by Mor-Yossef and Levy [11,12]. A second order accurate dual time stepping approach is adopted for time-accurate flow simulations.

3.1.1 Dual Time Stepping Residual Definition

Let $\hat{\boldsymbol{R}}^n$ be the right hand side operator of the first order implicit Euler time integration scheme at time step n:

$$\hat{\boldsymbol{R}}^n = -\left[\frac{\partial(\hat{\boldsymbol{E}}^c - \hat{\boldsymbol{E}}^d)^n}{\partial\xi} + \frac{\partial(\hat{\boldsymbol{F}}^c - \hat{\boldsymbol{F}}^d)^n}{\partial\eta} + \frac{\partial(\hat{\boldsymbol{G}}^c - \hat{\boldsymbol{G}}^d)^n}{\partial\zeta}\right] \tag{8}$$

where all the derivatives are approximated using the appropriate finite difference operators. For dual time stepping, the right hand side operator for sub-iteration k is given by:

$$\hat{\boldsymbol{R}}^k_{dt} = -\left[\frac{3\hat{\boldsymbol{Q}}^k - 4\hat{\boldsymbol{Q}}^n + \hat{\boldsymbol{Q}}^{n-1}}{2\Delta t} + \hat{\boldsymbol{R}}^n\right] \tag{9}$$

The k^{th} sub-iteration residual is calculated by summing the right hand side operator over the complete computational domain and all conservation equations:

$$L_2Norm = \sqrt{\sum_{\xi=1}^{\xi_{max}}\sum_{\eta=1}^{\eta_{max}}\sum_{\zeta=1}^{\zeta_{max}}\sum_{m=1}^{5}\hat{\boldsymbol{R}}^k_{dt}} \tag{10}$$

3.2 Aeroelastic Scheme

EZNSS solves the static or dynamic aeroelastic equation of motion (EOM) in modal coordinates. The dynamic EOM reads:

$$[GM]\{\ddot{\xi}\} + [GC]\{\dot{\xi}\} + [GK]\{\xi\} - \{GF_A(t)\} = 0 \tag{11}$$

and the static EOM reads:

$$[GK]\{\xi\} - \{GF_A(t)\} = 0 \tag{12}$$

where $\{\xi\}$ is the vector of modal displacements, $[GM]$, $[GC]$, and $[GK]$ are the generalized mass, damping, and stiffness matrices, respectively, and $\{GF_A(t)\}$ is the generalized aerodynamic force vector. The latter is calculated as:

$$\{GF_A(t)\} = [\Phi_A]\{F_A(t)\} \tag{13}$$

where $\{F_A(t)\}$ is the vector of aerodynamic forces provided at the computational surface mesh, and $[\Phi_A]$ is the modal matrix, in which each column holds a structural elastic mode, mapped to the computational surface mesh. The generalized mass and stiffness matrices and the modes matrix are generated by a finite-element code, and provided as inputs to the aeroelastic simulation. A spline routine, based on the Infinite Plate Spline (IPS) [13], is used to map the modes from the finite-element nodes in which they are computed to the CFD surface mesh.

In the dynamic aeroelastic case, the aeroelastic EOM is solved for the generalized displacements following each CFD time step. In the static case, the static aeroelastic EOM is solved following a user-defined number of CFD iterations, typically in the order of 100. This leads to an efficient aeroelastic scheme in which the elastic shape and the flow solution converge concurrently, while applying only a small number of elastic shape updates.

Following each solution of the aeroelastic EOM, the generalized deformations are used to compute the displacements at the computational surface grids, $\{u_A\}$, according to:

$$\{u_A\} = [\Phi_A]\{\xi\} \tag{14}$$

which are then mapped to the whole volume grid using a shearing method [14, 15].

3.3 Time Marching Scheme for the Dynamic Aeroelastic EOM

Since the generalized mass and stiffness matrices are diagonal, Eq. 11 can be written for each mode separately, as:

$$GM_{ii}\ddot{\xi}_i + 2\zeta GM_{ii}\sqrt{\Omega_i}\dot{\xi}_i + GM_{ii}\Omega_i\xi_i = GF_{A_i}(t) \tag{15}$$

where GM_{ii} is the i^{th} diagonal term of the generalized mass matrix, Ω_i and ζ_i are the i^{th} mode eigenvalue and structural damping coefficients, ξ_i is the generalized displacement, and GF_{A_i} is the associated aerodynamic generalized force.

Finite differences are used to evaluate the time derivatives of ξ. In addition, the equations are put in *delta form* so that only the increments are taken into account. This results in the following set of equations:

$$\Delta\ddot{\xi}_i + 2\zeta\sqrt{\Omega_i}\Delta\dot{\xi}_i + \Omega_i\Delta\xi_i = \frac{\Delta GF_{A_i}}{GM_{ii}} \tag{16}$$

One equation for each mode.

Prior to numerically solving the modal equations of motion, the system is rewritten in a state space formulation, as follows:

$$\begin{aligned} \Delta\dot{\xi}_i &= \Delta\eta_i \\ \Delta\dot{\eta}_i &= \frac{\Delta GF_{A_i}}{GM_{ii}} - 2\zeta\sqrt{\Omega_i}\Delta\eta_i - \Omega_i\Delta\xi_i \end{aligned} \tag{17}$$

The system can now be integrated using a standard Runge-Kutta method. The EZNSS code utilizes a 4^{th} order Runge-Kutta scheme to advance the solution in time. The aeroelastic and flow equations share the same time step, such that a single aeroelastic integration step is performed following each CFD time step.

4 THE BENCHMARK SUPERCRITICAL WING (BSCW) CONFIGURATION

The BSCW is a semi-rigid, semispan, rectangular wing, with a chord of 0.4064 m (16 inches), a span of 0.8128 m (32 inches), and a SC(2)0414 supersonic airfoil. The model has 40 pressure transducers to measure surface pressure distribution at the 60% span station, and 40 more at the 95% span station. [2]

The test cases for the AePW are based on two wind tunnel experiments of the BSCW that were conducted in the NASA Langley Transonic Dynamics Tunnel. The first experiment is a flutter test, in which the semi-rigid wing was suspended from a pitch and plunge apparatus (PAPA), simulating two degrees-of-freedom flutter [2] (The dynamic characteristics of the wing and mount system are provided in Ref. [16]). The BSCW was tested for flutter in air and in R-12 gas. Reference data (for AePW purposes) includes experimental results in R-12 gas, at *Mach 0.74, 0°AoA*, with fixed transition at 6.5% chord on both the upper and lower surfaces. Data includes the flutter dynamic pressure and frequency, unsteady surface pressure data while the model was at flutter, and steady pressure data for a fixed model (acquired with the PAPA locked). The second experiment is a forced excitation test, in which the wing was oscillated in pitch, about an axis at the 30% chord, via an oscillating turn table. [3] This experiment was performed in R-134a gas. Transition was fixed at 7.5% chord on both the upper and lower surfaces. Reference data includes unsteady pressure distribution in response to pitch excitation at two flow conditions: *Mach 0.7, 3°AoA*, and a more physically complex case at *Mach 0.85, 5°AoA*. Unforced pressure distributions are also available for these flow conditions. The current study includes flutter analysis about *Mach 0.85, 5°AoA*, although there was no flutter wind-tunnel test at these conditions. Table 1 summarizes the second AePW cases, and figure 2 (taken from Ref. [4]) summarizes the analysis input parameters for each case.

Two computational meshes of C-O type were used in this study, a nominal coarse mesh, and a medium mesh. The coarse mesh has dimensions of 253x71x99 in the chordwise, spanwise, and perpendicular directions, respectively, and the medium mesh has dimensions 361x110x138. For both meshes the far field extends approximately 90 chords away from the wing surface.

It is noted that in both the flutter and forced excitation cases, the wing was mounted on a large splitter-plate, suspended 40 inches off of the wind tunnel wall, as seen in figure 1. The PAPA / OTT mounts were located behind the splitter-plate. In all of the numerical simulations in this study the splitter-plate is modeled as an inviscid wall. Transition (fixed at 6.5% and 7.5% chord in the flutter and forced excitation tests, respectively) was not accounted for in the numerical simulations. Also, although the BSCW wing is semi-rigid (see Ref. [16]), flutter simulations were based only on the pitch and plunge motions of the wing on its mount.

Table 1: Second AePW analysis cases

	Case 1	Case 2	Case 3A	Case 3B	Case 3C
Mach	0.7	0.74	0.85	0.85	0.85
AoA	3^o	0^o	5^o	5^o	5^o
Dynamic Data Type	Forced oscillations	Flutter	Unforced; Unsteady	Forced oscillation	Flutter
Notes	OTT R134	PAPA R-12	OTT R134	OTT R134	No exp. data R134

Parameter	Symbol	Units	OTT Configuration	PAPA Configuration	OTT Configuration
Mach	M		0.7	0.74	0.85
AoA	α	deg	3°	0°	5°
Reynolds number (based on chord)	Re_c		4.560x10^6	4.450x10^6	4.491x10^6
Reynolds number per unit length	Re	Re_c/ft	3.456x10^6	3.338x10^6	3.368x10^6
Dynamic pressure	q	psf	170.965	168.800	204.197
Velocity	V	ft/s	387.332	375.700	468.983
Speed of sound	a	ft/s	553.332	506.330	552.933
Static temperature	T_{stat}	F	85.692	89.250	87.913
Density	ρ	$slug/ft^3$	0.00228	0.002392	0.001857
Ratio of specific heats	γ		1.113	1.136	1.116
Dynamic viscosity	μ	$slug/ft-s$	2.58x10^{-7}	2.69x10^{-7}	2.59x10^{-7}
Prandtl number	Pr		0.683	0.755	0.674
Test medium			R-134a	R-12	R-134a
Total pressure	H	psf	823.17		757.31
Static pressure	p	psf	629.661		512.120
Purity	X	%	95	95	95
Ref. molecular weight based on 100% purity	M	g/mol	102.03	120.91	102.03
Sutherland's constant	C	R	438.07	452.13	438.07
Reference viscosity	μ_{ref}	$lb-sec/ft^2$	2.332x10^{-7}	2.330x10^{-7}	2.332x10^{-7}
Reference temperature	T_{ref}	R	491.4	491.4	491.4

Figure 2: BSCW analysis input parameters (taken from Ref. [4])

5 RESULTS

5.1 Case 2 - Flutter, Mach 0.74, 0°AoA, R-12

5.1.1 Static Analysis, Mach 0.74, 0°AoA, R-12

Figure 3 presents pressure coefficient distributions at two span sections, computed in a static analysis at Mach 0.74, 0°AoA, with the SST, TNT, and SA turbulence models. All of the analyses converged well to steady state solutions (figure 4), yielding pressure distributions similar to the experimental data. These converged flow fields served as the starting conditions for flutter simulations. The analysis using the SA model was repeated on a *medium mesh*. Pressure coefficient distributions in Figure 5 show that this case is not sensitive to the mesh density. Further simulations were therefor performed on the coarse mesh.

5.1.2 Structural Model

The structural model of the BSCW wing has two modes, a plunge mode and a pitch mode, about the center chord. Table 2 presents the frequencies, stiffness, and inertia properties of the model. Figure 6 shows the modes mapped to the CFD surface mesh.

Table 2: Structural modal properties

	Frequency (Hz)	Generalized Stiffness (Nm)	Generalized Mass (kgm^2)
Plunge	3.3	437.7	1.0
Pitch	5.2	1067.3	1.0

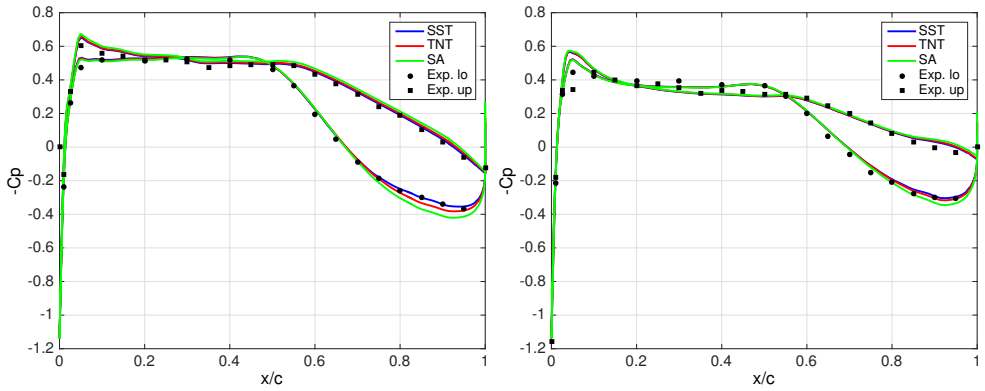

(a) 0.6 span (b) 0.95 span

Figure 3: Pressure coefficient at two span stations; Various turbulent models; Mach 0.74, 0°AoA

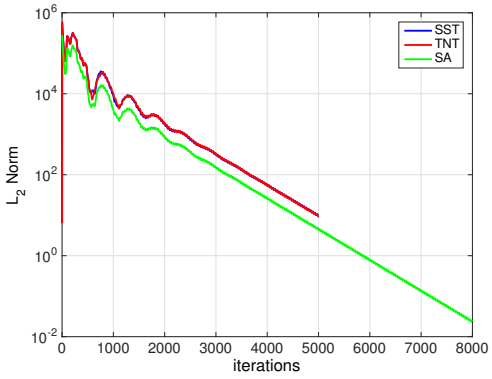

Figure 4: Convergence plot; Various turbulent models; Mach 0.74, 0°AoA

5.1.3 Linear Flutter Analysis, Mach 0.74

Linear flutter analysis was conducted using ZAERO ZONA6 linear panel method. The wing was divided to 8x16 panels along the chord and span respectively. Figure 7 shows $\omega - V - g$ plot from linear analysis. The computed flutter speed is 112 m/s, corresponding to dynamic pressure of 7560 Pa (158 psf, compared to 169 psf from the wind tunnel experiment), and the flutter frequency is 4.3 Hz (identical to the experimental flutter frequency). The good prediction of the flutter speed by the linear model indicates that, at least for this mildly non-linear case, the linear solution could serve as an initial guess of the flutter point.

5.1.4 Flutter Simulation, Mach 0.74, 0°AoA, R-12

Dynamic aeroelastic simulation was conducted in EZNSS, where the dynamic pressure was set to the experimental flutter dynamic pressure. The nominal computational parameters were: Coarse mesh, physical time step of 2e-4 s (which corresponds to about 1200 time steps per flutter cycle), SA turbulence model, and convergence requirement of five OOM residual drop in the sub-iterations, between each two consecutive time steps. The aeroelastic simulation was started from the converged flow field on the *rigid* configuration. The flow field about the rigid configuration is different than that on the elastic configuration, hence providing the perturbation required to get the flutter solution started. Figure 8 presents the wing tip displacement and twist during the flutter simulation, showing a slow growth of the displacements, which is typ-

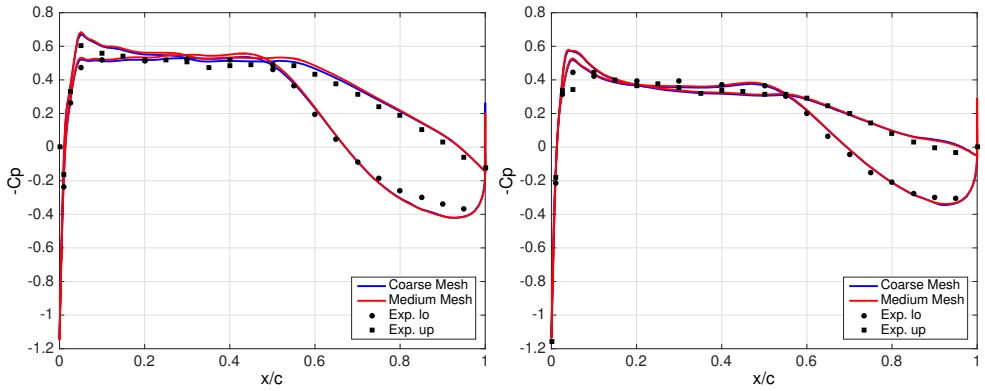

(a) 0.6 span (b) 0.95 span

Figure 5: Pressure coefficient at two span stations; SA model; Coarse and medium mesh; Mach 0.74, 0° AoA

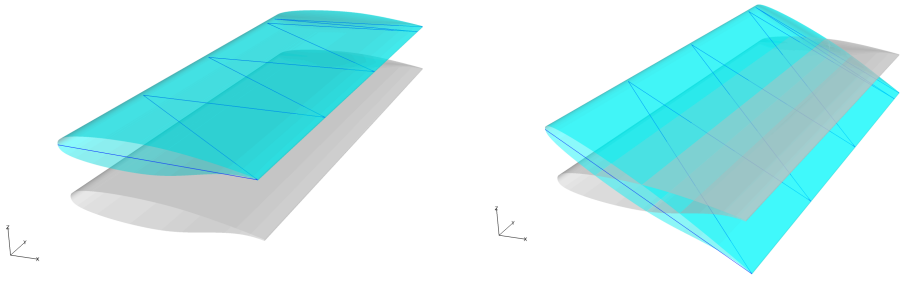

(a) Heave mode -3.32 Hz (b) Pitch mode - 5.25 Hz

Figure 6: Modes mapped to the CFD surface mesh

ical of dynamic pressure slightly above flutter. The simulated oscillation frequency is 4.2 Hz, compared to 4.3 Hz measured in the experiment.

Figures 9 and 10 show the transfer function (TF) between the pressure coefficient in the 60% span station (upper and lower wing surfaces) and the wing tip pitch angle, at a frequency of 4.4 Hz, close to the flutter frequency. The TF in figures 9 and 10 was computed based on short data, of about 7000 iterations, with snapshots of the flow field taken following every 50 iterations, thus making the Fourier analysis resolution coarse (1.47 Hz). Considering the short data used to compute the TF, the simulation captures the unsteady pressure during flutter accurately.

The simulation was repeated with structural damping coefficient of 0.03 (Eq. 15). Simulated wing tip displacements and twist, figure 11, show that with this amount of damping the system is at the flutter point (approximately). It is noted, however, that the test model is supposed to have as little as 0.001 structural damping coefficient [16], hence the simulation is somewhat under-predicting the flutter dynamic pressure.

5.1.5 Effect of Computational Parameters

Figure 12 shows the modal heave and pitch displacements that were computed using different time steps. It is clear that the results converge with decreasing time step. Based on these simulations a time step of 2e-4 s was selected as the nominal time step for the aeroelastic simulations. In order to study the significance of convergence in the sub-iterations, three simulations

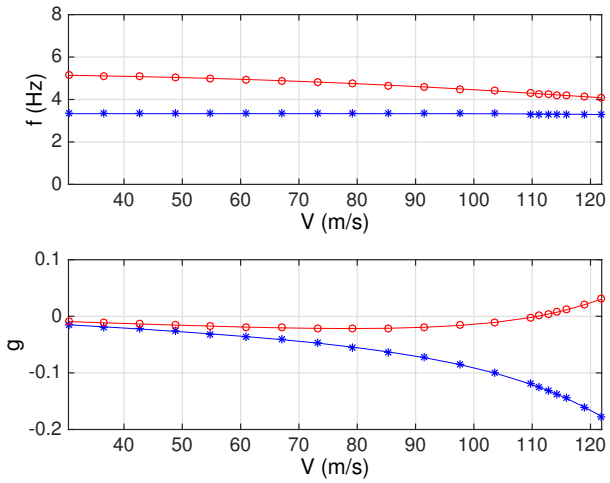

Figure 7: Linear flutter analysis using ZAERO linear panel method ZONA6

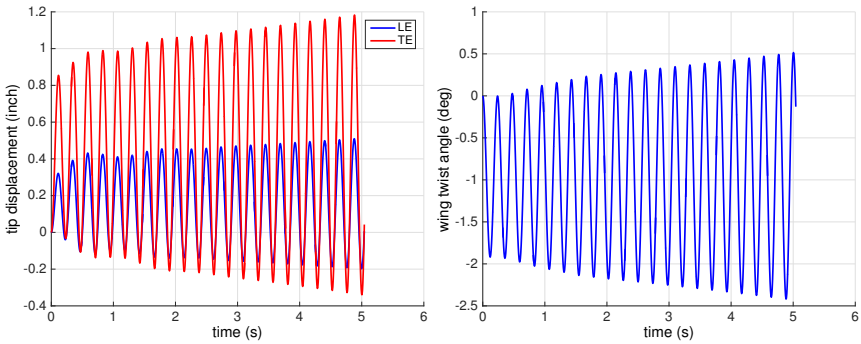

(a) Tip displacement (b) Wing twist

Figure 8: Wing tip displacement and twist during flutter simulation, no structural damping; Mach 0.74, 0°AoA; SA model

were performed, with residual drop cutoffs of 3, 5, and 7 OOM. Figure 13 shows that the less converged solution was slightly decaying, while the more converged solutions were diverging (flutter), thus indicating the significance of temporal convergence.

The aeroelastic simulation was repeated with the SST and TNT turbulence models, using the nominal computational setup. All turbulence models yielded similar, slightly diverging aeroelastic responses (figure 14).

5.1.6 Flutter Dynamic Pressure Estimation Based on Aerodynamic ROM

Aeroelastic simulation, as described in the previous sub-section, can provide accurate information on the aeroelastic behavior at certain user-defined flow conditions, but it cannot provide an estimate of the flutter speed. For this, a frequency domain reduced-order model (ROM) of the unsteady aerodynamic forces was identified, based on computed responses to prescribed modal motions. The ROM assumes that the aerodynamic system (geometry and flow conditions) is a black box. The system is excited mode by mode, and the generalized forces are computed and recorded. A frequency domain ROM of the system's generalized aerodynamic forces is generated by computing the transfer function between the generalized forces (the output) and the modal excitations (the input). The details of the ROM methodology are presented in Ref. [5].

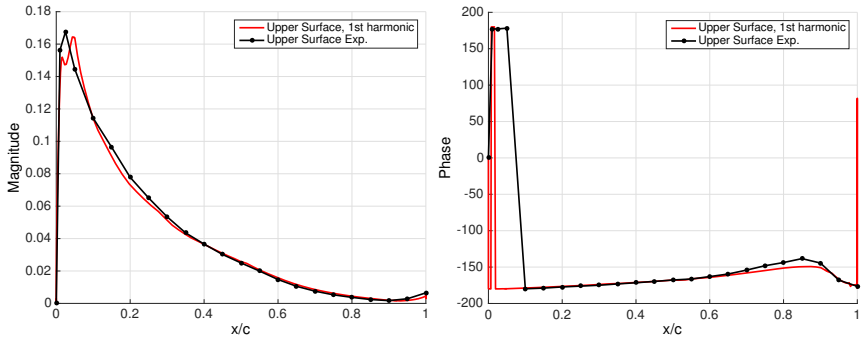

(a) Magnitude (b) Phase

Figure 9: Transfer function between Cp on the upper surface and the wing tip twist angle during flutter; Mach 0.74, 0°AoA; SA model

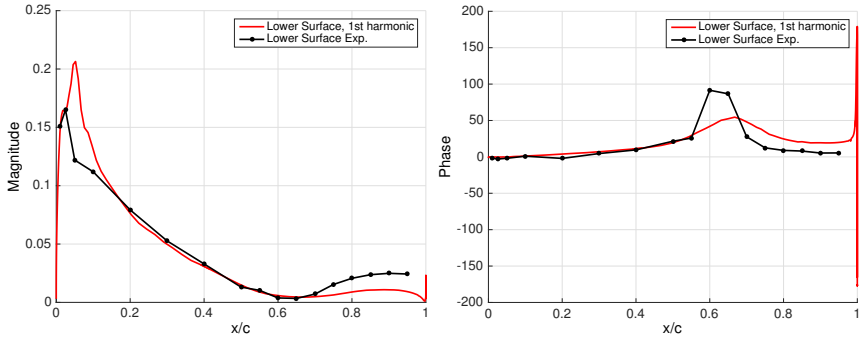

(a) Magnitude (b) Phase

Figure 10: Transfer function between Cp on the lower surface and the wing tip twist angle during flutter; Mach 0.74, 0°AoA; SA model

To generate the ROM, two separate CFD simulations were launched, to compute the generalized aerodynamic forces that develop in response to prescribed modal excitations in the heave and pitch modes. The prescribed modal motion is that of a white noise, filtered to include frequencies up to 12.5Hz (we recall that the system's natural frequencies are 3.32 and 5.25 Hz). The max heave modal amplitude was set to 0.5, corresponding to physical displacement of 0.05 m, and the max modal pitch amplitude was set to 0.1, corresponding to 0.05 rad. The excitation amplitudes for ROM generation should be sufficient to excite the system, yet not too large as to result in nonlinear response (due to separated flow and stall).

Generalized aerodynamic force coefficient matrices (GAFs) were computed by

$$GAF(k) = \frac{P_{\xi GF_A}(k)}{P_{\xi\xi}(k)} \tag{18}$$

where $P_{\xi GF_A}(k)$ is the cross spectral density of the input (prescribed modal motion) and output (generalized force in a mode), and $P_{\xi\xi}(k)$ is the power spectral density of the input. [5] The simulations of responses to prescribed modal motions were carried out for about 8000 time steps, using physical time step of dt=2e-3, thus resulting in a fine frequency resolution of 6.2e-2 Hz (reduced frequency of 6.9e-04). These simulations were performed with a less stringent convergence requirement of 3 OOM.

Figure 15 shows the GAF matrices (real and imaginary parts) as a function of reduced frequency.

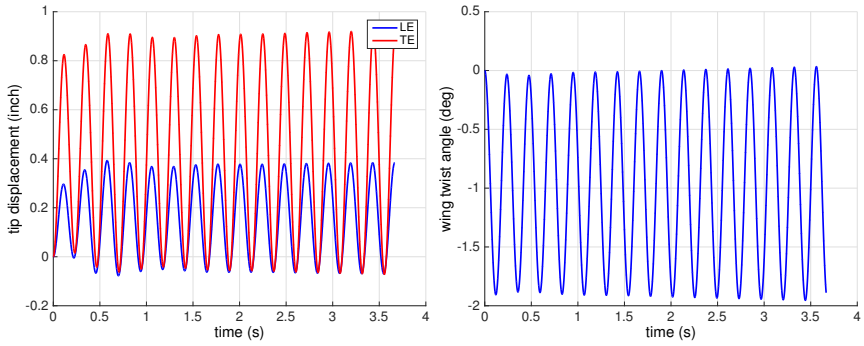

(a) Tip displacement (b) Wing twist

Figure 11: Wing tip displacement and twist during flutter simulation, 3% structural damping; Mach 0.74, 0°AoA; SA model

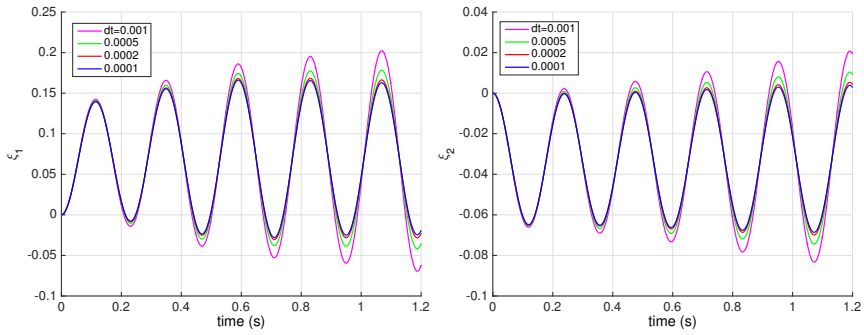

(a) Heave (b) Pitch

Figure 12: Modal displacement during flutter; Mach 0.74, 0°AoA; SA model, coarse mesh; Time step effect

The GAF matrix i,j term stands for the generalized force coefficient in the i^{th} mode due to modal motion of the j^{th} mode. The plot presents GAF matrices for reduced frequency values up to $k = 0.1$. We recall that the prescribed modal excitations were limited to physical frequencies up to 12.5Hz, corresponding to reduced frequency of 0.138, which is therefore the highest reduced frequency value for which a ROM can be identified in this case. This low range of reduced frequencies is suitable for the problem at hand, in which the flutter frequency (4.3 Hz) corresponds to a reduced frequency of 0.047. Figure 15 also presents GAF values computed by ZAERO ZONA6 panel method. For this case the linear and CFD-based GAF matrices are quite similar.

Figure 16 shows the coherence between the generalized aerodynamic forces and the modal motions as a function of frequency. Although coherence values are low for the very low frequencies, for the frequency range of interest, between the first and second elastic mode frequencies, coherence values are close to 1, thus the identified ROM is expected to be accurate.

Figure 17 shows $\omega - V - g$ plot computed with the ROM, using the k-method, compared to results from ZAERO. The flutter in this case is mild, with very shallow crossing. Thus small variations in the GAF values (between the CFD-based ROM and the ZAERO linear panel method) result in a relatively large difference in the flutter speed, making it difficult to pinpoint the flutter speed. The ROM based flutter speed is 122 m/s, and the corresponding dynamic pressure is 8678 Pa (181 psf, compared to 169 psf from the wind tunnel experiment).

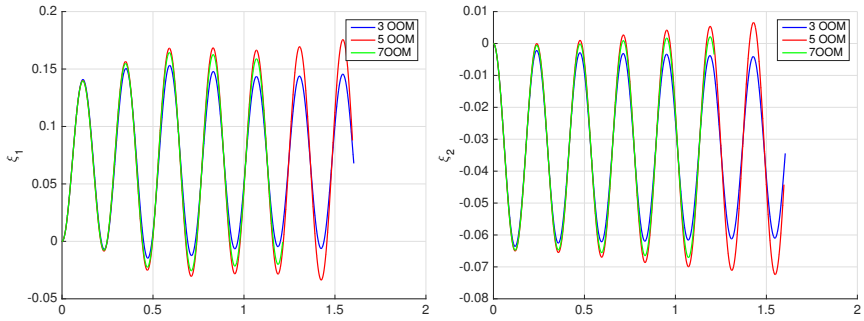

(a) Heave (b) Pitch

Figure 13: Modal displacement during flutter; Mach 0.74, 0°AoA; SA model, coarse mesh, dt=2e-4 s; Temporal convergence effect

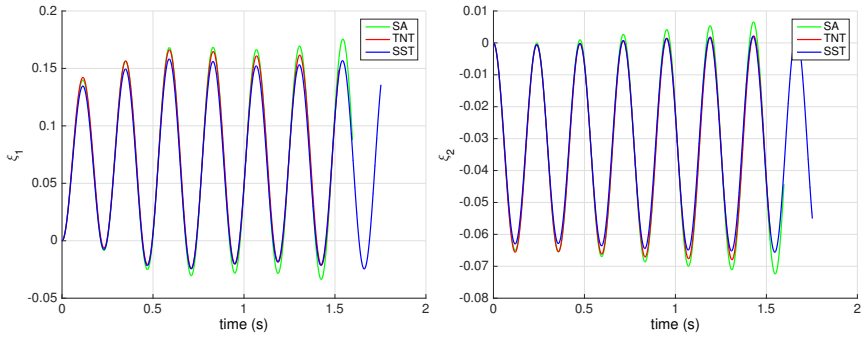

(a) Heave (b) Pitch

Figure 14: Modal displacement during flutter; Mach 0.74, 0°AoA; Coarse mesh, dt=2e-4 s; Various turbulence models

As mentioned earlier, ROM generation requires two additional simulations to compute the generalized aerodynamic forces in response to prescribed modal motions in each of the two modes of the problem. The accuracy and resolution of the ROM, as well as its computational cost, depend on the length of these simulations (the length of the training data). Figure 18 shows $\omega - V - g$ plot computed with GAFs that are based on simulations of 2048, 1024, and 512 iterations. The corresponding reduced-frequency resolution of the resulting GAFs ranges between 2.69e-3 for the long training data, to 2.15e-2 for the shortest. In this case, the effect on flutter speed prediction is minor, as shown in figure 18. That is, the additional runs required to generate the training data for the ROM can be very short, making this ROM methodology an efficient tool for flutter prediction.

5.2 Case 3A - Static Analysis, Mach 0.85, 5°AoA, R-134a

Figure 19 shows results of static analysis at Mach 0.85, 5°AoA, computed with the SST and SA turbulence models. In the wind tunnel experiment the flow at these conditions was slightly unsteady, with shock oscillations between about 40% to 50% chord location, as captured by the pressure transducers at 60% span station (see figure 7 of Ref. [3]). In the current study, all of the simulations converged to steady flows. Figure 19(a) shows the computed static pressure coefficient at 60% span station, compared to the experimental mean pressure values. While the SST model captures well the upper-surface shock location, none of the models were able to capture the pressure values at the recovery area behind the shock, on both the upper and

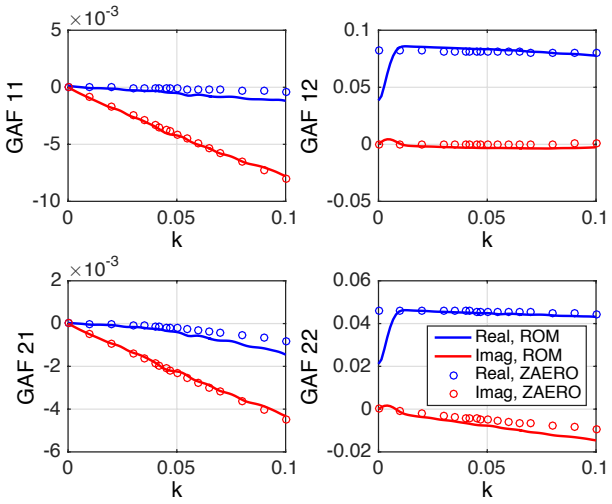

Figure 15: GAF ROM; Mach 0.74, 0°AoA

lower surfaces. Repeating the simulations with the medium mesh did not improve the prediction significantly, as shown in figure 20. Similar results were also presented by other AePW analysts - see figures 3(b) and 5(b) of Ref. [1].

5.3 Case 3C - Flutter, Mach 0.85, 5°AoA, R-134

5.3.1 Flutter Dynamic Pressure Estimation Using Aerodynamic ROM, Mach 0.85, 5°AoA, R-134

This case is a blind test, without reference flutter data from wind tunnel experiments. The approach in this case was to estimate the flutter dynamic pressure using a ROM for the unsteady aerodynamic forces, following the same methodology that was presented in Case 2, and to validate it by dynamic aeroelastic simulation.

To generate the ROM, two separate CFD simulations were conducted to compute the generalized aerodynamic forces that develop in response to prescribed modal excitations in the heave and pitch modes. The simulations were computed at Mach 0.85, 0°AoA. As in Case 2, the prescribed modal motion is that of a white noise, filtered to include frequencies up to 12.5Hz. The simulations were carried out for about 7000 time steps, using physical time step of dt=2e-3, thus resulting in a frequency resolution of about 0.07 Hz. Figure 21 presents the coherence between the generalized aerodynamic forces and the modal motions as a function of reduced frequency, showing coherence values close to 1 for the frequency range of interest. Figure 22 shows the GAF matrices (real and imaginary parts) as a function of reduced frequency, compared to GAF

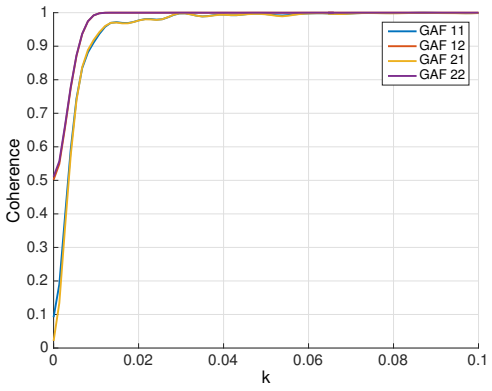

Figure 16: Coherence between GAFs and prescribed modal motion; Mach 0.74, 0°AoA

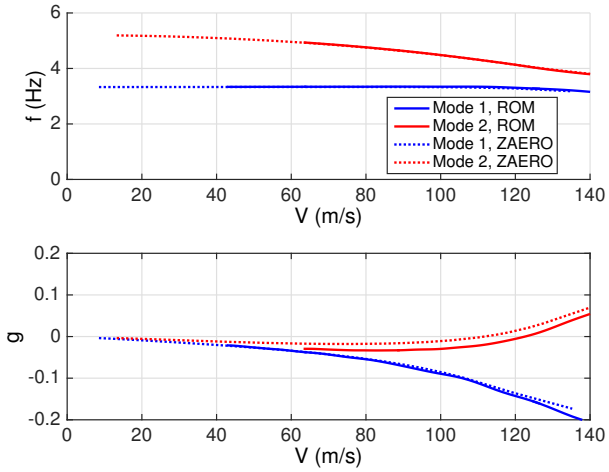

Figure 17: ROM-based flutter analysis; Mach 0.74, 0°AoA

values computed by ZAERO ZONA6 panel method. As expected, for this transonic, nonlinear case linear aerodynamics fails to predict the unsteady aerodynamic forces.

Figure 23 shows $\omega - V - g$ plot computed with the ROM, using the k-method, compared to results from ZAERO. Linear aerodynamics is not expected to provide a good estimation of the flutter speed. Linear based results are presented here only in order to get a feel for how remote they are from the ROM-based estimation. The ROM based flutter speed is 180 m/s, and the corresponding dynamic pressure is 16500 Pa (345 psf).

Unlike in the Mach 0.74 flutter case, in this case the ROM accuracy does depend significantly on the length of the training data, and so does the predicted flutter speed. Figure 25 shows $\omega - V - g$ plot computed with GAFs that are based on simulations of 7000, 4096, and 2048 iterations, showing that the predicted flutter speed changes between the different ROMs. It is also likely that the quality of the ROM, and the corresponding flutter prediction, depend on the accuracy of the training data. In this case the convergence requirement in the sub-iterations was set to 3 OOM. It is possible that higher convergence requirement would result in a more accurate ROM. However, the computational cost of ROM generation would increase as well. This was not tested in this study.

Since the flow conditions are nonlinear, and angle of attack dependent, a ROM was also generated about 5°AoA. Figure 24 shows $\omega - V - g$ plot computed with the two ROMs. Although

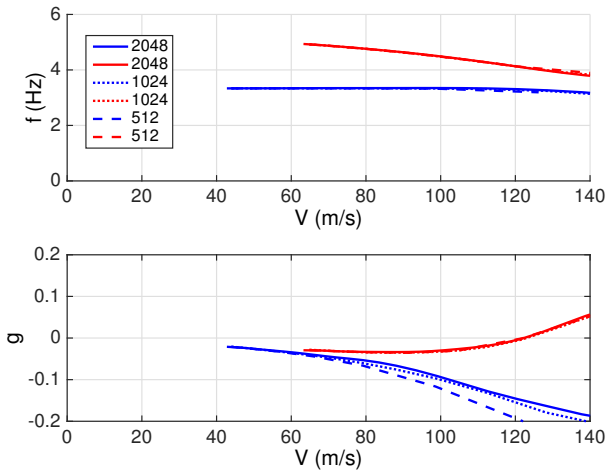

Figure 18: ROM-based flutter analysis - various length of training data; Mach 0.74, 0°AoA

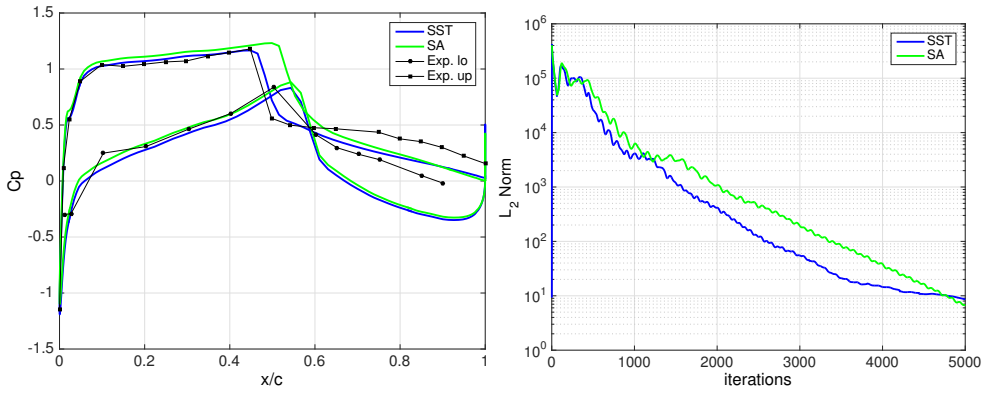

(a) Cp (b) Convergence

Figure 19: Pressure coefficient at span station 0.6 (a) and convergence plot (b); Mach 0.85, 5°AoA

the starting static flow fields are different, it did not make a significant effect on the predicted flutter point.

To verify the predicted flutter speed, an aeroelastic simulation was launched at dynamic pressure of 16500 Pa. The computational parameters are similar to those detailed in section B.4, and the simulation was performed with the SST turbulence model. Figure 26 presents the simulated wing tip responses, showing that while the heave response is decaying, the pitch response is on the verge of flutter, with very little damping. The response frequency is $4.8Hz$.

6 SUMMARY

Flutter prediction and simulations were performed with the EZNSS flow solver for the second Aeroelastic Prediction Workshop (AePW). For Case 2, at Mach 0.74, 0°AoA, aeroelastic simulation was presented at the experimental flutter dynamic pressure, and the response was found to be slightly diverging. Parametric study presented the effects of time step, temporal convergence, computational mesh and turbulence modeling on the simulated aeroelastic response. Linear flutter analysis showed that for this mildly non-linear case linear aerodynamic modeling is suitable for flutter speed prediction. A reduced-order model for the unsteady aerodynamic forces was generated, based on CFD responses to modal excitation. The unsteady aerodynamic

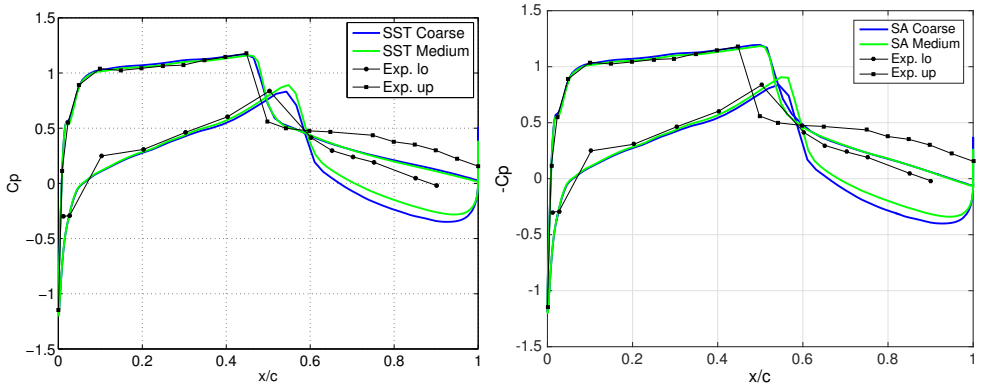

(a) SST (b) SA

Figure 20: Mesh effect on pressure coefficient at span station 0.6; SST (a) and SA (b) models; Mach 0.85, 5° AoA

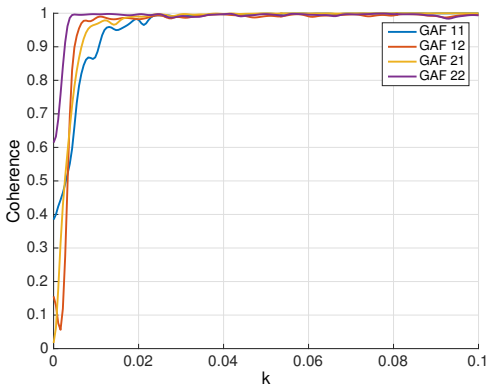

Figure 21: Coherence between GAFs and prescribed modal motion; Mach 0.85, 0° AoA

ROM was used to predict the flutter speed. For this case the flutter is mild and the crossing is shallow, thus small changes in the generalized aerodynamic force coefficient matrices can result is relatively large changes in the predicted flutter speed. However, all models (linear and ROM) are capable of predicting the flutter speed.

For Case 3, Mach 0.85, 5° AoA, in which the experiment showed some unsteadiness, flow simulations resulted in a steady flow. None of the turbulence closures were able to accurately predict the pressure recovery behind the shock. Flutter analysis for Case 3 was based on a ROM, and since the flutter dynamic pressure is not available from test data, the predicted flutter speed was verified in an aeroelastic simulation. Overall, the aeroelastic simulations based on Reynolds-Averaged Navier-Stokes were able to predict the aeroelastic response at flutter conditions, even in complex flow conditions for which the static flow simulation failed to accurately predict the shock and separated boundary layer features.

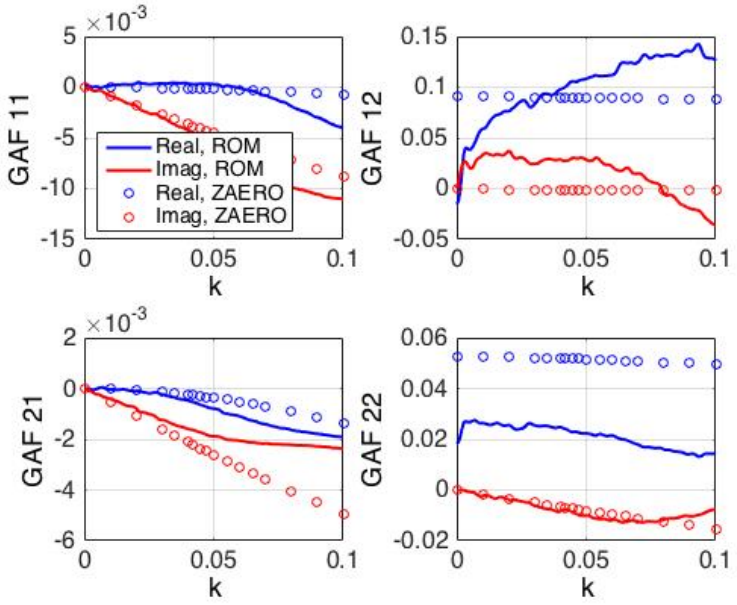

Figure 22: GAF ROM; Mach 0.85, 0° AoA

7 REFERENCES

8 REFERENCES

[1] Heeg J., Chwalowski P., Schuster D., and Dalenbring M. Overview and lessons learned from the aeroelastic prediction workshop. In *54th AIAA/ASME/ASCE/AHS/ASC Structures, Structural Dynamics, and Materials Conference*, Boston, MA, April 2013. AIAA 2013-1798.

[2] Dansberry B., Durham M., Bennett R., Rivera J, Silva W.A., Wieseman C., and Turnock D. Experimental unsteady pressures at flutter on the supercritical wing benchmark model. In *34th AIAA/ASME/ASCE/AHS/ASC Structures, Structural Dynamics, and Materials Conference*, April 1993. AIAA 93-1592.

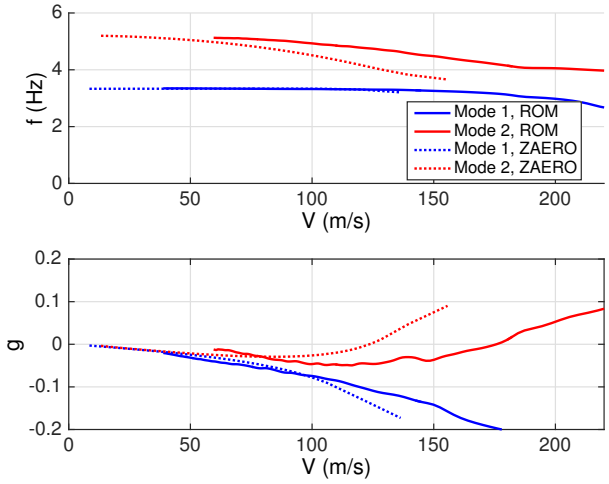

Figure 23: ROM-based flutter analysis; Mach 0.85, 0° AoA

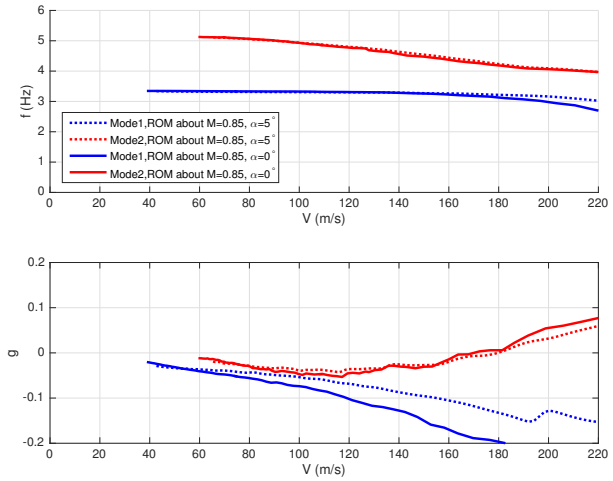

Figure 24: ROM-based flutter analysis; ROMs computed about Mach 0.85, 0°AoA, and Mach 0.85, 5°AoA

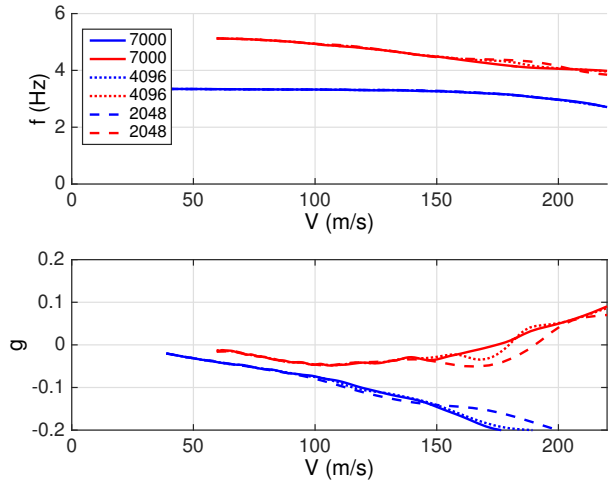

Figure 25: ROM-based flutter analysis - various length of training data; Mach 0.85, 0°AoA

[3] Heeg J. and Piatak D.J. Experimental data from the benchmark supercritical wing wind tunnel test on an oscillating turntable. In *54th AIAA/ASME/ASCE/AHS/ASC Structures, Structural Dynamics, and Materials Conference*, Boston, MA, April 2013. AIAA 2013-1802.

[4] Heeg J., Chwalowski P., Raveh D. E., Dalenbring M. J., and Jirasek A. Plans and example results for the 2nd aiaa aeroelastic prediction workshop. In *56th AIAA/ASME/ASCE/AHS/ASC Structures, Structural Dynamics, and Materials Conference*, April 2015. AIAA 2015-0437.

[5] Raveh D. E. Identification of Computational-Fluid-Dynamics Based Unsteady Aerodynamic Models for Aeroelastic Analysis. *Journal of Aircraft*, 41(3):620–632, 2004.

[6] F. R. Menter. Zonal two equation k-ω turbulence models for aerodynamic flows. In *24rd AIAA Fluid Dynamics Conference*, Orlando, FL, July 1993. AIAA paper 93 - 2906.

[7] C. Kok, Johan. Resolving the dependence on freestream values for the k-ω turbulence model. *AIAA Journal*, 38(7):1292–1295, 2000.

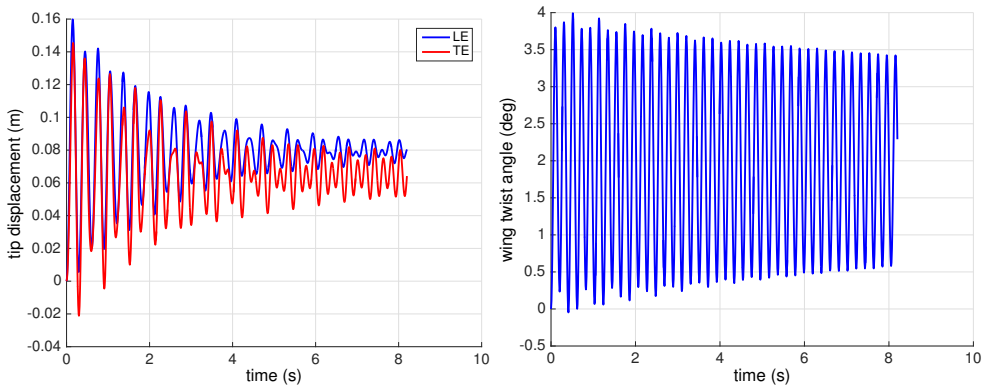

(a) Tip displacement (b) Wing twist

Figure 26: Wing tip displacement and twist during flutter simulation, Mach 0.85, 5°AoA; SST model

[8] Jack R. Edwards and Suresh Chandra. Comparison of eddy viscosity-transport turbulence models for three-dimensional, shock-separted flow fields. *AIAA Journal*, 34(4):756–763, 1996.

[9] P. Batten, M. A. Leschziner, and U. C. Goldberg. Average-state Jacobians and implicit methods for compressible viscous and turbulent flows. *Journal of Computational Physics*, 137(1):38–78, 1997.

[10] Meng-Sing Liou. A sequel to AUSM, part II:AUSM$^+$-up for all speeds. *Journal of Computational Physics*, 214(1):137–170, 2006.

[11] Y. Mor-Yossef and Y. Levy. The unconditionally positive-convergent implicit time integration scheme for two-equation turbulence models: Revisited. *Computers & Fluids*, 38(10):1984–1994, 2009.

[12] Y. Mor-Yossef and Y. Levy. Designing a positive second-order implicit time integration procedure for unsteady turbulent flows. *Computer Methods in Applied Mechanics and Engineering*, 196(41-44):4196–4206, 2007.

[13] Harder R. L. and Desmarais R. N. Interpolation Using Surface Splines. *Journal of Aircraft*, 9(2):189–191, 1972.

[14] Schuster D. M. Vadyak J. and Atta E. Static Aeroelastic Analysis of Fighter Aircraft Using a Three-Dimensional Navier-Stokes Algorithm. *Journal of Aircraft*, 27(5):820–825, 1990.

[15] Raveh D. E., Levy Y., and Karpel M. Structural Optimization Using Computational Aerodynamics. *AIAA Journal*, 38(10):1974–1982, 2000.

[16] Dansberry B., Durham M., Turnock L., Silva W.A., and Rivera J.A. Physical Properties of the Benchmark Models Program Supercritical Wing. In *NASA TM-4457*, 1993.

COPYRIGHT STATEMENT